Available online at www.sciencedirect.com

jmr&t Journal of Materials Research and Technology

journal homepage: www.elsevier.com/locate/jmrt

Original Article

Achieving superior low-temperature toughness in high-strength low-carbon steel via controlling lath boundary segregation

Xinghao Wei [a], *Lixin Sun* [a,**], *Zhongwu Zhang* [a,b,*], *Yang Zhang* [a], *Junhua Luan* [c], *Zengbao Jiao* [d], *Chain Tsuan Liu* [c], *Gang Zhao* [b]

[a] *Key Laboratory of Superlight Materials and Surface Technology, Ministry of Education, College of Materials Science and Chemical Engineering, Harbin Engineering University, Harbin 150001, China*

[b] *State Key Laboratory of Metal Material for Marine Equipment and Application, Iron & Steel Research Institute of Ansteel Group Corporation, Anshan 114009, Liaoning, China*

[c] *Department of Materials Science and Engineering, City University of Hong Kong, Hong Kong, China*

[d] *Department of Mechanical Engineering, The Hong Kong Polytechnic University, Hong Kong, China*

ARTICLE INFO

Article history:
Received 23 October 2022
Accepted 14 March 2023
Available online 18 March 2023

Keywords:
Low-temperature toughness
Lath boundary segregation
Strengthening mechanism
Cu precipitation strengthening

ABSTRACT

The optimal aging temperatures of 400–550 °C for high strength steels falls into the dangerous temperature range of temper-embrittlement. To obtain a good low-temperature toughness, temperatures above 600 °C are usually selected for aging treatments, resulting in a huge loss of strength. In this work, the effects of aging treatments at 500 and 550 °C on the impact performance of a Cu precipitation-strengthened steel at a low temperature of −80 °C were systematically investigated. The solute segregation at lath boundaries is found to be the main factor controlling the low-temperature toughness. Excellent impact performance of ~180 J at −80 °C along with a high yield strength of ~1050 MPa and a total elongation of 19% can be obtained by controlling the segregation of solute elements, specifically Mo and Mn at the lath boundaries. The evolutions of matrix and precipitates during aging treatments were investigated. The strengthening and toughening mechanisms are also critically discussed.

1. Introduction

High-strength low-carbon (HSLC) steels are critical in engineering applications, such as automotive, shipbuilding, and construction industries [1–6]. Cu-precipitation strengthening is one of the most effective methods for low-carbon steels to achieve high strength, high toughness, and excellent weldability [7–9]. The mechanical properties of precipitation-

* Corresponding author. Key Laboratory of Superlight Materials and Surface Technology, Ministry of Education, College of Materials Science and Chemical Engineering, Harbin Engineering University, Harbin, China.
** Corresponding author.
E-mail addresses: lxsun@imr.ac.cn (L. Sun), zwzhang@hrbeu.edu.cn (Z. Zhang).

https://doi.org/10.1016/j.jmrt.2023.03.110

strengthened steels are highly dependent on the microstructures of precipitation, including the particle size, number density, morphology, and distribution [10,11]. Cu-precipitation can provide more than 720 MPa of yield strength at the peak aging state, however, the strengthening capability declines significantly with the coarsening of precipitates and the decrease of number density when overaged [12,13].

Tempering is a typical heat treatment process that is used to improve the ductility and toughness of martensitic steels, but often at the expense of strength. In general, the optimal aging/tempering temperature at 400–550 °C for most precipitation-strengthened steels falls into the dangerous temperature range of temper embrittlement [7,14–18]. Brittle failures of tempered high-strength steels are usually attributed to temper-embrittlement (TE) and tempered martensitic embrittlement (TME) [19–22]. TE is usually considered a result of the segregation of impurity elements, such as P, Sb, Sn, S and As, at the prior austenite grain boundaries [23]. The segregation causes an intergranular fracture, which can be eliminated by high-temperature tempering and fast quenching (>600 °C) [24]. TME generally refers to the decomposition of martensite into Fe_3C in the intra-lath region, which usually leads to transgranular fracture and is irreversible [22]. In HSLC steels, by reducing the content of carbon and other impurity elements, the precipitation of coarse-sized Fe_3C and segregation of impurity elements can be avoided. However, brittle fracture still occurs after tempering at 400–550 °C, and the mechanism of the embrittlement remains controversial [11,25]. Many researchers choose to increase the aging temperature to avoid this range. However, this approach would lead to the rapid growth of Cu precipitates and hence the great degradation of the strengthening capability. Another way is that a critical quenching process is applied before aging treatments for obtaining a small amount of retained austenite to increase the toughness. However, this approach also reduces the strength and raises the production costs [25–27].

The segregation of some solute elements on grain boundaries can improve the impact toughness of steels. The segregation of element B on prior austenite grain boundaries can effectively reduce the grain boundaries energy and enhance the cohesion of the boundary [28,29]. Yoo et al. found that Mo can segregate on the prior austenite grain boundaries and inhibit grain boundary cracking, effectively reducing the occurrence of intergranular fracture [30,31]. However, these studies mainly pointed out the effects of element segregated on the prior austenite grain boundaries on toughness and the inhibition of intergranular transformation. The solute element segregation at lath boundaries and their effects on the transgranular cleavage fracture were seldomly reported. Therefore, it is of technically necessity to understand the mechanism of temper embrittlement via a systematical investigation on the microstructural evolution of both the matrix, specifically lath boundaries and Cu-precipitates in the aging process to achieve a high toughness without sacrificing the strength.

In this study, we developed a nano-Cu precipitation-strengthened steel with a combination of high strength, good ductility, and excellent low-temperature toughness by delicately controlling microstructures of the matrix and Cu-precipitates. Particularly, the segregation of solute elements at the martensitic lath boundaries and its effects on the toughness were thoroughly investigated.

2. Experimental

The composition of the nano-Cu precipitation-strengthened steel was measured using optical emission spectroscopy and is reported in Table 1. The steel was fabricated by melting in a vacuum induction furnace under an argon atmosphere. The cast ingot was then homogenized at 1150 °C for 2 h and hot rolled to 25 mm in thickness, followed by water quenching. The hot-rolled samples were solution-treated firstly at 820 °C for 30 min, followed by water quenching. The as-quenched samples were aged at 500 and 550 °C for different periods of time, followed by water quenching.

The Vickers hardness measurement were conducted using an applied load of 500 g for 15s. Each reported microhardness value is an average of 10 measurements and the error is the standard deviation. Tensile tests were carried out on an INSTRON 5565 testing machine at 25 °C with a strain rate of 0.001 s^{-1}. Two specimens were tested for each condition, and the error is determined by the standard deviation of the average. The 0.2% offset method was taken to estimate the yield strength. The Charpy V-notch impact tests were performed on a Zwick/Roell 450 J instrumented impact machine with ASTM E23 standards. The specimens were immersed in a bath composed of a mixture of anhydrous alcohol and liquid nitrogen at −80 °C for more than 20 min before impacting. Three samples were impacted for each condition, and the error was determined by the standard deviation.

Electron backscattered diffraction (EBSD) and transmission electron microscopy (TEM) were used to analyze the microstructure. The grain boundary and crystallographic orientation of the samples were characterized by Hitachi S3400 scanning electron microscope (SEM), which is equipped with an EBSD detector. A step size of 0.3 μm was used for the EBSD scan, and the post-treatment of the obtained data was conducted using the HKL Channel 5 software. The phase components of the samples were characterized by PANalytical X'Pert Pro X-ray diffractometer (XRD). Cu K_a target was selected for the XRD tests with a step size of 0.02°. TEM specimens were prepared by the focused ion beam (FIB) technique in an FEI Scios scanning electron microscope (SEM). The thickness of the FIB samples is around 50 nm. The TEM characterizations were conducted on a JEM 2100F microscope under an operating voltage of 200 kV. The high-angle annular dark-field imaging (HAADF) and energy dispersive X-ray (EDX) spectroscopy were carried out on a Titan G2 60–300 aberration-corrected TEM operated at 300 kV. The number densities of Cu precipitates and carbides were estimated based on the counted number of precipitates in TEM images and the corresponding measured area and the thickness of the FIBed samples. The number densities of both the Cu precipitates and carbides were also verified by atom probe tomography results.

Atom probe tomography (APT) characterizations were performed in a local electrode atom probe (Cameca LEAP 5000 XR). Data acquisition was performed at a low temperature of

Table 1 – Chemical composition of the steel. (wt.%).

Fe	Cu	Ni	Mn	Si	Mo	Cr	Nb + Ti	C	Als	P	S
Bal.	2.1	6.0	0.9	0.2	0.5	0.5	0.04–0.07	0.04	0.02	0.005	0.0007

50 K with a pulse repetition rate of 200 kHz and a pulse fraction of 20%. The Imago Visualization and Analysis Software (IVAS) version 3.8 was employed for creating the 3-dimensional (3D) reconstructions and data analysis.

3. Results

3.1. Mechanical properties

The hardness and low-temperature impact toughness profiles of the steel aged at 500 and 550 °C are shown in Fig. 1 as a function of aging time. The age hardening and over-aged softening take place at both temperatures. The hardness of the steel reaches a peak value after aging for 0.2 h at 550 °C, faster than that aged at 500 °C. The as-quenched steel exhibits an excellent impact toughness with an impact energy of about 170 J. However, the impact energy decreases rapidly at the early stage of aging. The minimum impact energy appears at the peak-age hardening state for both temperatures. Then the impact energy increases with the increase in aging time. When the aging time exceeds 10 h at 500 °C, the impact energy decline again.

Tensile stress-strain curves of the steel after aging for 30 min and 100 h at 500 °C (500/30 min and 500/100 h, respectively) and 2 h at 550 °C (550/2 h) are shown in Fig. 2. The yield strength of the 500/30 min sample is 1163 ± 28 MPa. It has the highest strength, but its impact energy is only 20 ± 3 J. With a long-term aging for 100 h, the yield strength decreases to 969 ± 3 MPa, while the impact energy is still very low, only 18 ± 9 J. For the 550/2 h sample, the yield strength is 1048 ± 4 MPa, and the impact energy is 177 ± 11 J, showing an excellent combination of high strength and toughness.

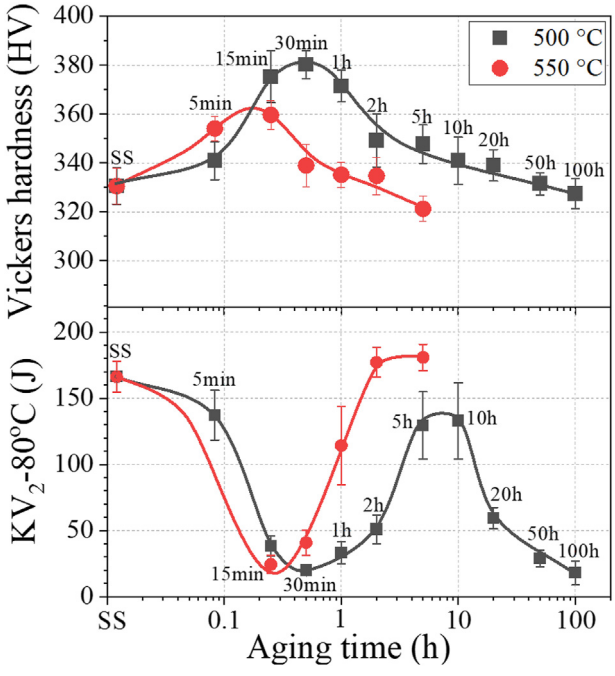

Fig. 1 – Microhardness and impact energy versus aging time at 500 °C and 550 °C.

3.2. Microstructure characterization

To investigate the mechanism of embrittlement and de-embrittlement in this steel, systematical microstructure characterizations were conducted. Fig. 3 shows the XRD patterns of the 500/30 min, 500/100 h, and 550/2 h samples, confirming that all samples consist of a single BCC structure. No austenite or precipitation phases can be detected through XRD.

The SEM images and Charpy impact fracture surfaces of the 500/30 min, 500/100 h, and 550/2 h samples are shown in Fig. 4. The SEM images (Fig. 4a–c) reveal that all the samples have a lath martensite morphology. Quasi-cleavage transgranular fractures appear in the fractography of 500/30 min (Figs. 4d) and 500/100 h (Fig. 4e) samples, while dimple-like features, the characteristics of ductile failure in the 550/2 h sample (Fig. 4f). Intergranular fracture caused by conventional tempering brittleness are not observed in this steel. These observations are consistent with the Charpy impact results.

Detailed microstructures of the 500/30 min, 500/100 h, and 550/2 h samples were investigated by EBSD and TEM, as shown in Fig. 5. The multi-leveled microstructure with prior-austenite grains, packets, blocks, and laths in the EBSD inverse polar figures (IPF) (Fig. 5a–e) conform with the similar microstructures of lath martensite for all the three samples. Generally, the boundaries of packets and blocks are high angle grain boundaries (HAGBs, black lines in Fig. 5a–c), which can

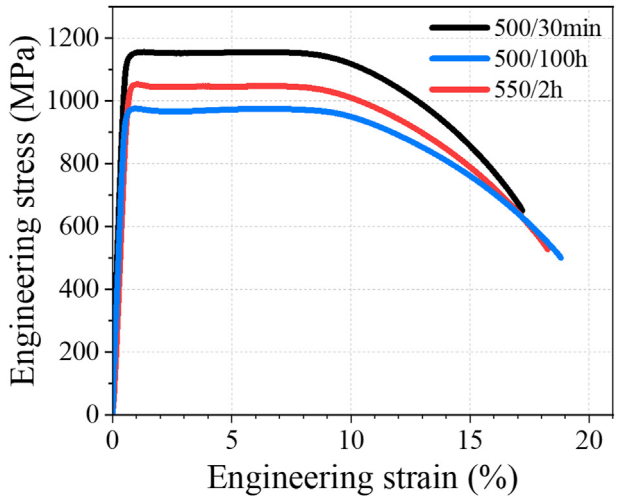

Fig. 2 – Engineering stress-strain curves of typical states.

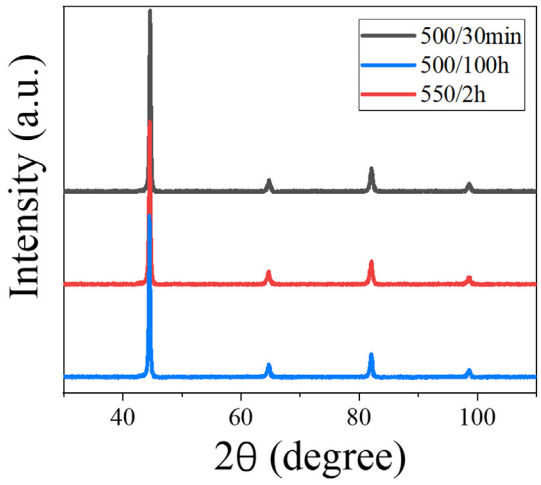

Fig. 3 – The X-ray diffraction patterns of 500/30 min, 500/100 h, and 550/2 h.

effectively hinder the propagation of cracks [32]. Therefore, the size of 'blocks' is considered as the effective grain sizes (EGS) in lath martensite [32–34]. Fig. 5d–f presents the bright-field TEM micrographs of the three samples. Typical lath-type martensitic microstructures can be seen clearly, indicating that the aging treatments did not change the lath structures at the three states.

The corresponding misorientation angle distribution, local misorientation angle distribution, and EGS distribution are shown in Fig. 6. The HAGBs content of the 500/30 min, 500/100 h, and 550/2 h samples (Fig. 6a–c) are 45.2%, 44.8%, and 47.5%, respectively, showing no obvious differences. The EGS of the 500/30 min, 500/100 h, and 550/2 h samples (Fig. 6g) are 3.14 ± 0.15, 3.41 ± 0.18, and 3.19 ± 0.11 μm, respectively. With the aging time increasing from 30 min to 100 h at 500 °C, the EGS increased by 8.6%, indicating that the aging time has little effect on the EGS. The change of density of geometric necessary dislocations (GND), which are mainly depend on the value of local misorientation (Θ), can be calculated by Refs. [35,36]:

$$\rho_{GND} = \frac{2\Theta}{ub} \quad (1)$$

where u is the scanning step length 300 nm, and b is the Burgers vector 0.248 nm. Θ was obtained from the local misorientation profile in Fig. 6d–f. The calculated ρ_{GND} of the 500/30 min, 500/100 h, and 550/2 h samples are 5.81 × 10^{14}, 5.42 × 10^{14}, and 5.54 × 10^{14} m^{-2}, respectively.

To explore the effects of aging treatments on the chemistry of lath boundaries, the EDS elemental mappings of lath boundary were carried out for the 500/30 min, 500/100 h, and 550/2 h samples, as shown in Figs. 7–9, respectively. It can be found that in the 500/30 min sample (Fig. 7), there is Ni and Mn segregation at the lath boundary. Meanwhile, a large number of fine Cu-precipitates are dispersed in the lath interior and boundaries, which would be the cause for the high yield strength. In the 550/2 h sample (Fig. 9), the segregation of Ni and Mn at lath boundaries decreases, while the Mo segregation occurs at the lath boundaries. The Cu-precipitates in the lath and lath boundary coarsen, resulting in the reduction of yield strength. In the 500/100 h sample (Fig. 8), the segregation of Mo on the grain boundary disappears, and the segregation of Ni and Mn is obvious. The number density of Cu-precipitates decreases significantly.

Fig. 10 shows the concentration profiles across the lath boundaries in the 500/30 min, 500/100 h and 550/2 h samples. The results are consistent with the EDS elemental mappings in Figs. 7–9. The Cu segregation in the 500/30 min sample is due to the formation of Cu precipitate on the lath boundary. It is found that Mn segregates on the lath boundary at the early stage of aging, which results in a low toughness (Fig. 1). With the prolonged aging time, Mo begins to gradually segregate at

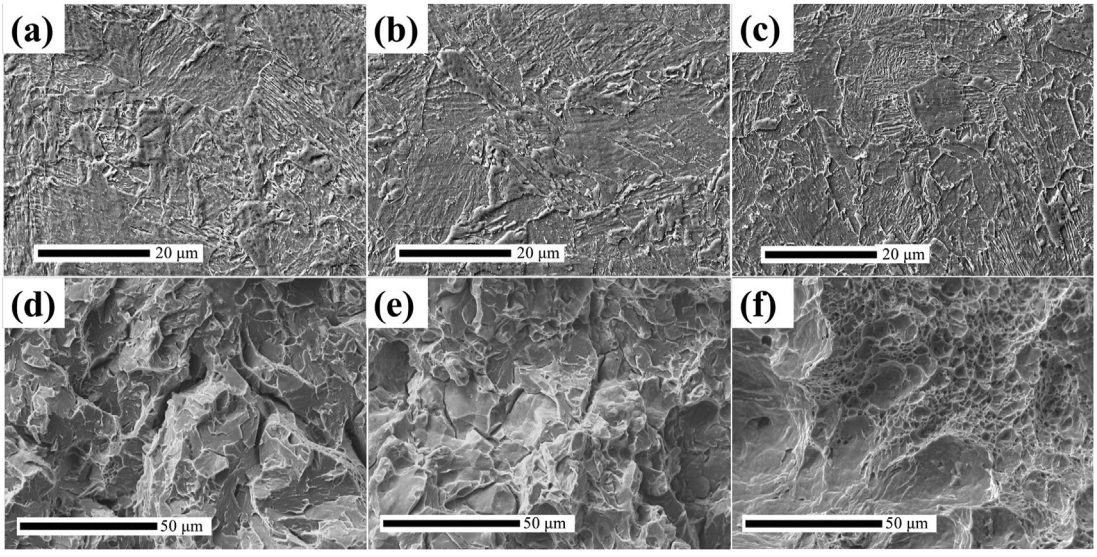

Fig. 4 – SEM micrographs of (a) 500/30 min, (b) 500/100 h, and (c) 550/2 h. The fracture surfaces of Charpy impact in the samples (d) 500/30 min, (e) 500/100 h and (f) 550/2 h, respectively.

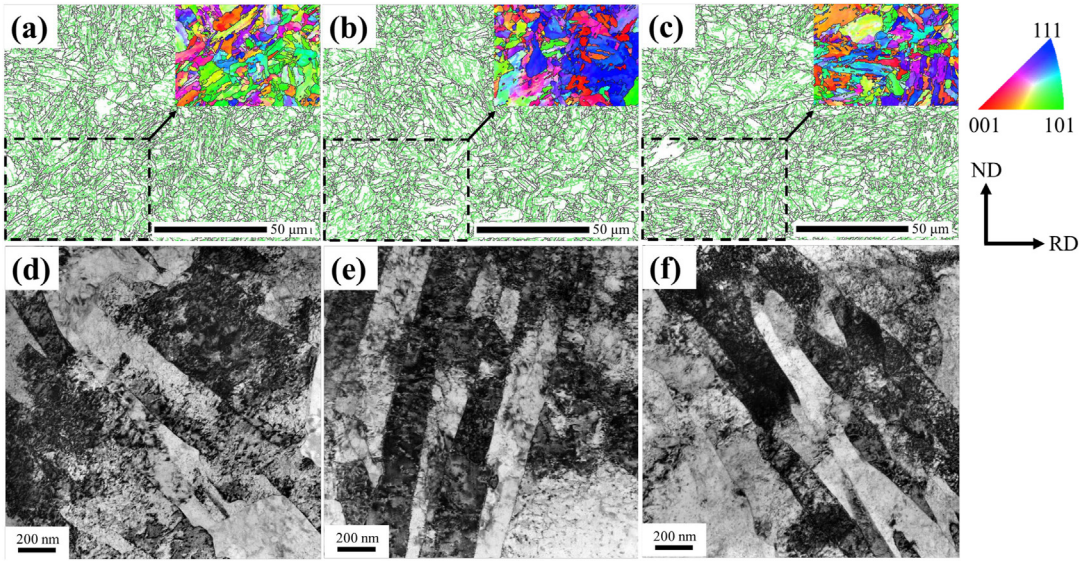

Fig. 5 – IPF and bright-field TEM images: (a) IPF, 500/30 min, (b) IPF, 500/100 h, (c) IPF, 550/2 h, (d) TEM, 500/30 min, (e) TEM, 500/100 h, and (f) TEM, 550/2 h.

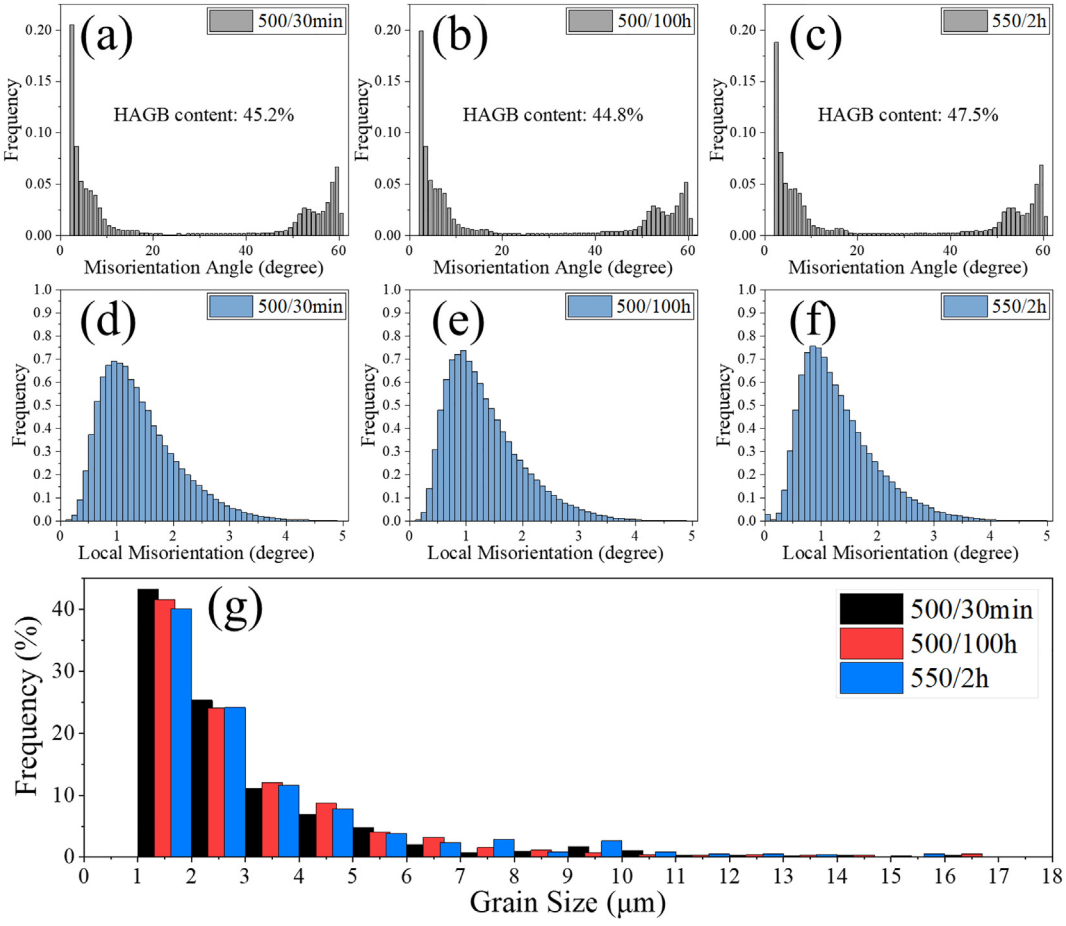

Fig. 6 – Corresponding misorientation angle distributions and local misorientation angle distributions of (a) (d) 500/30 min, (b) (e) 500/100 h, and (c) (f) 550/2 h; and EGS distributions (g).

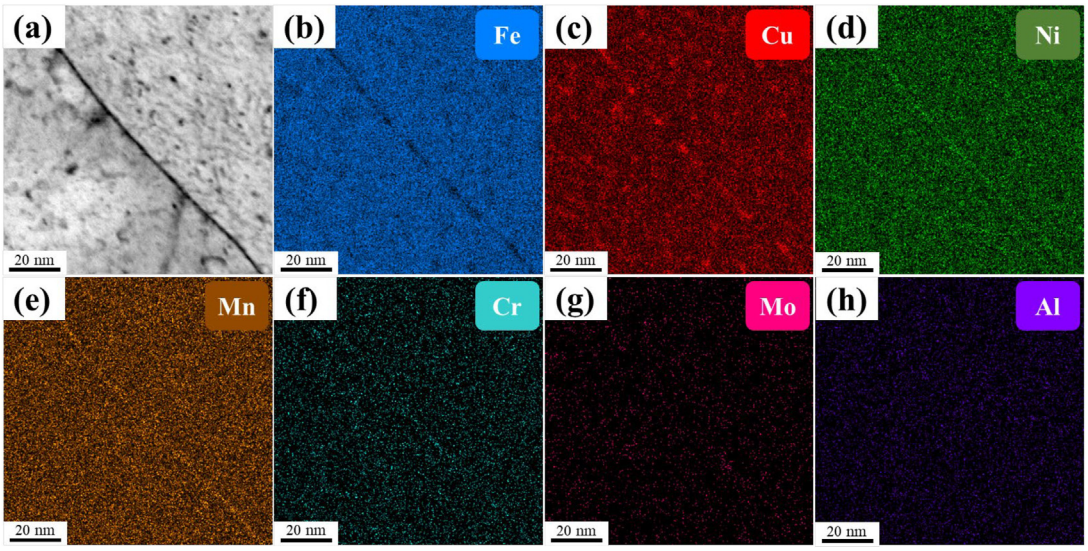

Fig. 7 – The EDS element mapping of the lath boundary in the 500/30 min sample.

grain boundaries, leading to a significant increase in toughness. When the aging time is extended to 100 h at 500 °C, the content of Mo element on the grain boundary decreases, the content of Mn and Ni elements increases, and the toughness decreases again.

Fig. 11 shows the Cu maps and HAADF images of the 500/30 min, 500/100 h, and 550/2 h samples along the $[0\ 0\ 1]_{bcc}$ axis. The size and the number density of the Cu precipitates in the 500/30 min sample (Fig. 10a) are approximately 1–3 nm and $9.8 \times 10^{23}/m^3$, respectively. The weak contrast changes and lattice coherence make precipitates difficult to be identified in HRTEM (Fig. 11d). Intense B2 ordered spots from the (0 1 0) B2 axis can be identified in the FFT patterns acquired from the precipitates (the inset of Fig. 11d). For the 500/100 h sample, the size of the Cu-precipitates is 8–20 nm, while the number density is $2.1 \times 10^{22}/m^3$. The shape of the precipitates changed from spherical to rod-like, and the structure changes from the B2 to FCC structure. The precipitates in the 550/2 h sample are larger than that in the 500/30 min sample, which are 4–9 nm is size, and the number density is $2.2 \times 10^{23}/m^3$. The two FFT patterns were extracted from the precipitates: one is the (0 1 0) B2 ordered point of a fine Cu-precipitate, and the other is a coarse precipitate with a FCC structure.

To accurately measure the composition and morphology of the precipitates, APT characterizations were carried out. Cu precipitates and Carbides are delineated by 10 at.% Cu iso-concentration and 5 at.% (C + Mo + Cr) iso-concentration surfaces of the 500/30 min, 500/100 h, and 550/2 h samples are displayed in Fig. 12, respectively. The 500/30 min sample has a high number density of fine Cu-precipitates: the average

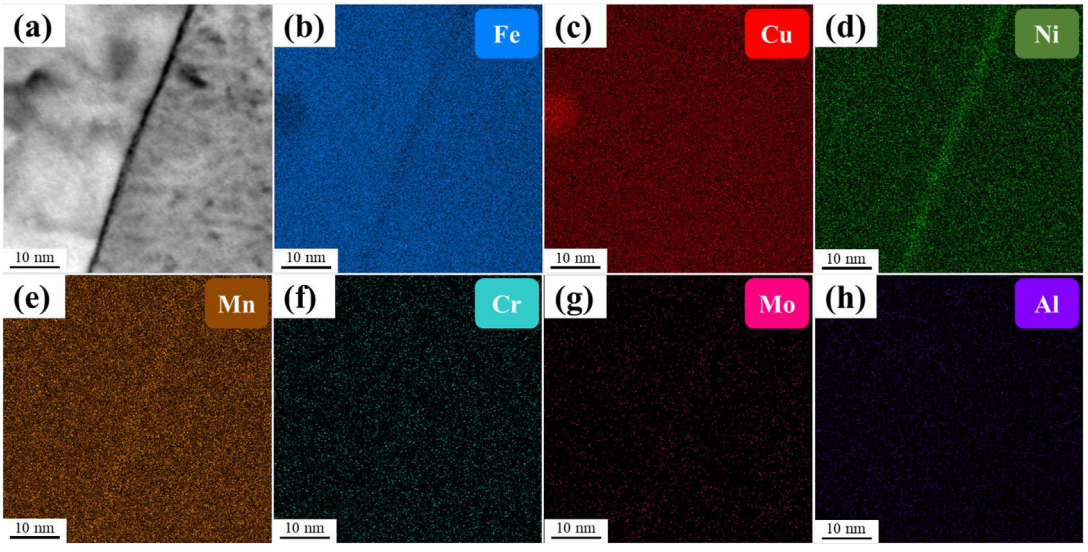

Fig. 8 – The EDS element mapping of the lath boundary in the 500/100 h sample.

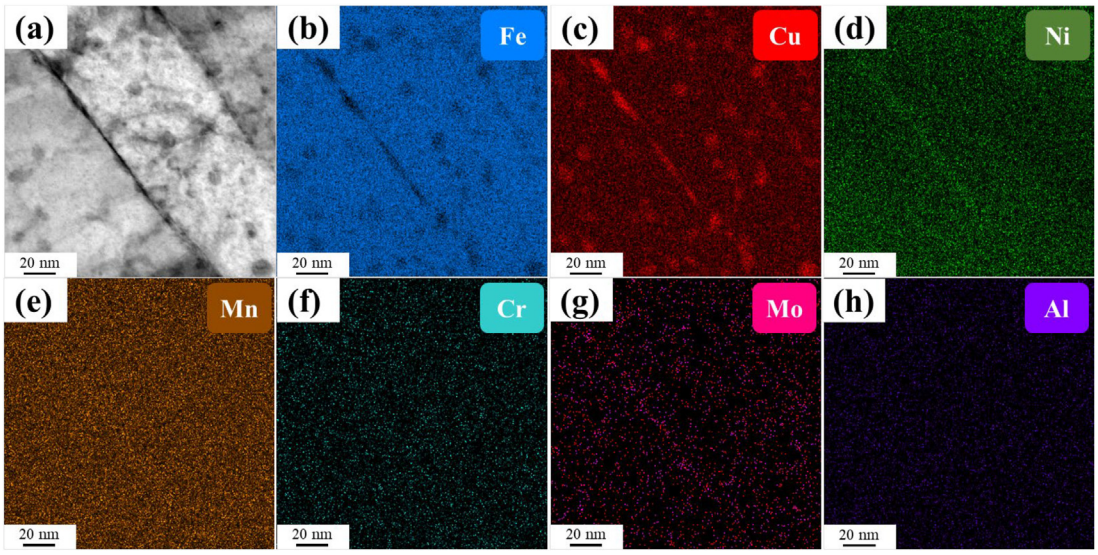

Fig. 9 – The EDS element mapping of the lath boundary in the 550/2 h sample.

size of ~1.4 ± 0.3 nm in radius and number density of $1.16 \times 10^{24}/m^3$. In the 500/100 h sample, the Cu-precipitates grow into platelet-like, and the effective radius of a sphere with the same volume is calculated to be ~6.8 nm. The carbides are also observed in the reconstruction and their average radius is ~2.9 ± 0.4 nm. Based on the number density and average size of carbides, the volume fraction can be estimated as 0.5%. This may be the main reason for the decrease of Mo content at the lath boundary of the 550/100 h sample. The radius of Cu-precipitates in the 550/2 h sample grows to

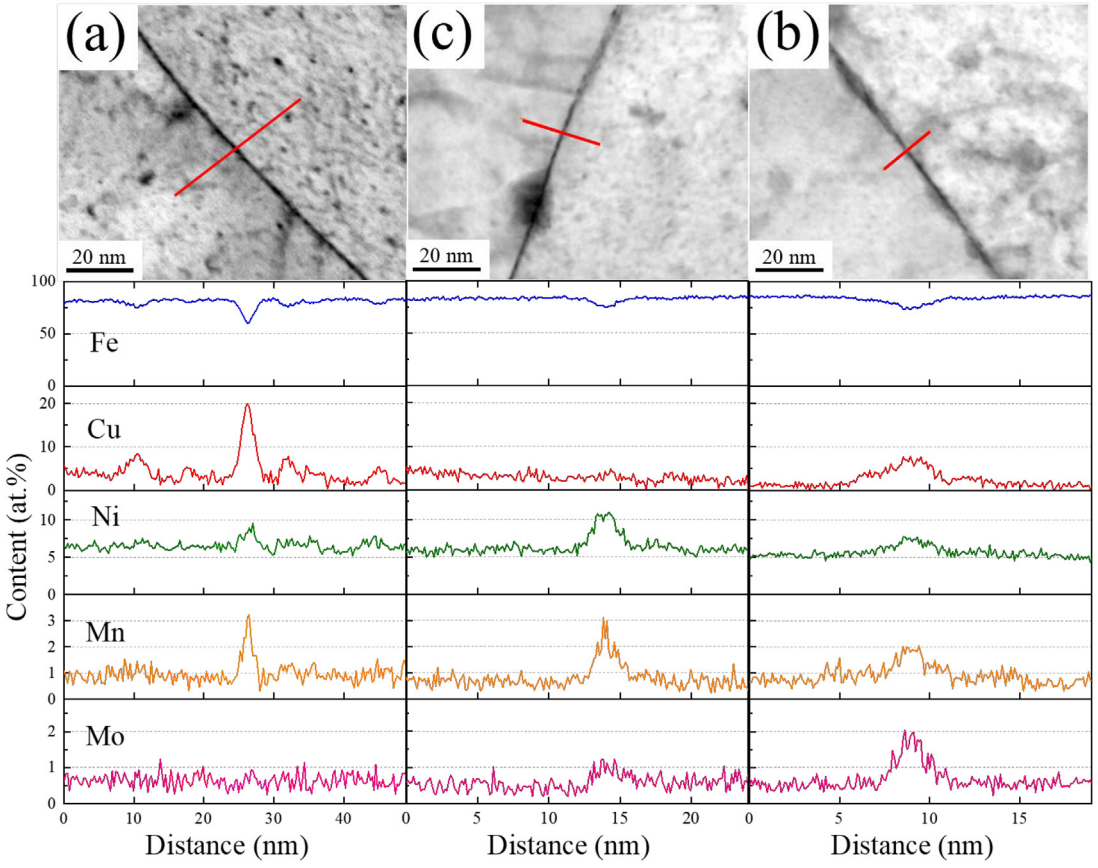

Fig. 10 – Concentration profiles across the lath boundary in the (a) 500/30 min, (b) 500/100 h, and (c) 550/2 h samples (above image shows the line scan across the lath boundary).

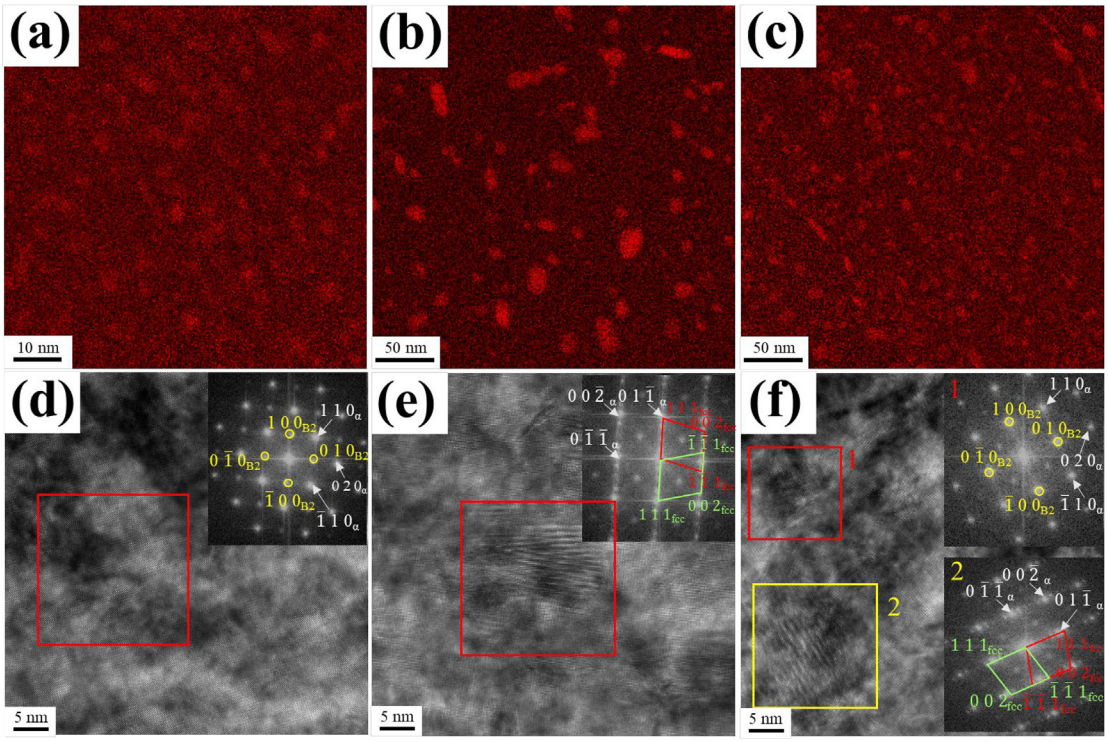

Fig. 11 – EDS element mapping and [0 0 1]$_{bcc}$ HRTEM image of the Cu-precipitates in (a), (d) 500/30 min, (b),(e) 500/100 h, and (c) (f) 550/2 h samples.

2.8 ± 0.4 nm, and the number density decreases to 1.2 × 10^{23}/m^3. In addition to spherical precipitates, rod-shaped precipitates were also observed. The volume fraction of Cu-precipitates in the 500/30 min, 500/100 h, and 550/2 h samples were calculated to be 1.2%, 2.8%, and 1.9%, respectively.

The proximity histograms of Cu precipitates and carbides for the 500/30 min, 500/100 h, and 550/2 h samples are shown in Fig. 13. The proximity histogram direction of these particles was marked with red cylinder in Fig. 12. The surface of Cu-precipitates is enriched with Ni. The Cu content in the core of fine Cu-precipitates is ~60% in the 500/30 min sample and exceeds 80% in the 500/100 h and 550/2 h samples. The composition of the carbides in the 500/100 h sample is 49.2Mo–8.8Cr–29.5C–2.8Fe–7.1Ni–1.1Mn–1.1Cu–0.35Si in at.%, as shown in Fig. 12d. Similar M_2C carbides have also been reported in other steels [11].

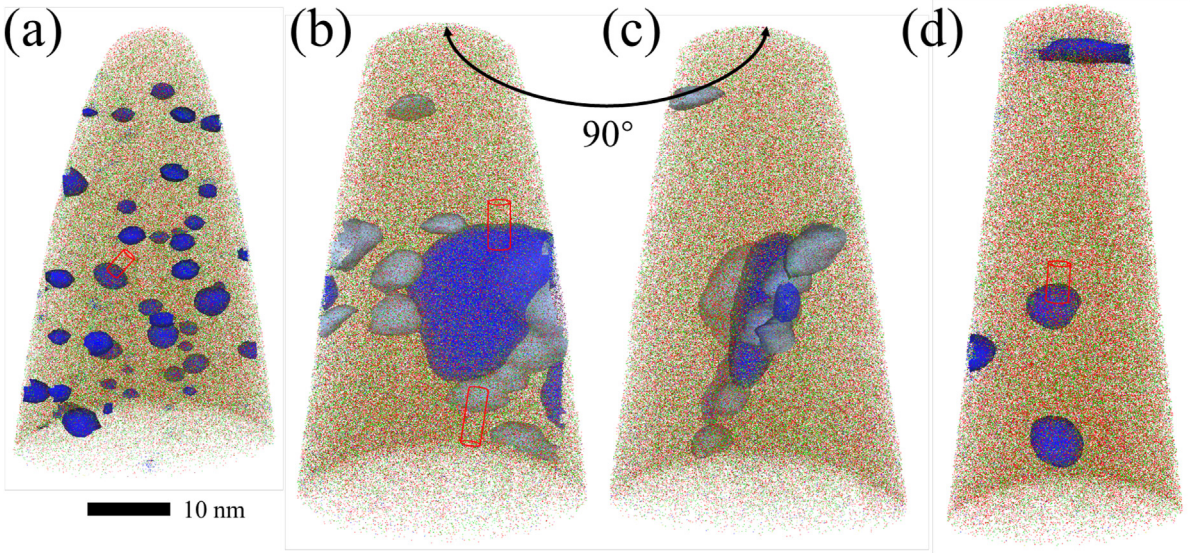

Fig. 12 – APT 3D reconstructions of 10 at.% Cu iso-concentration surfaces in (a) 500/30 min, (b), (c) 500/100 h, and (d) 550/2 h samples. The proximity histogram of carbides in (d) 500/100 h sample.

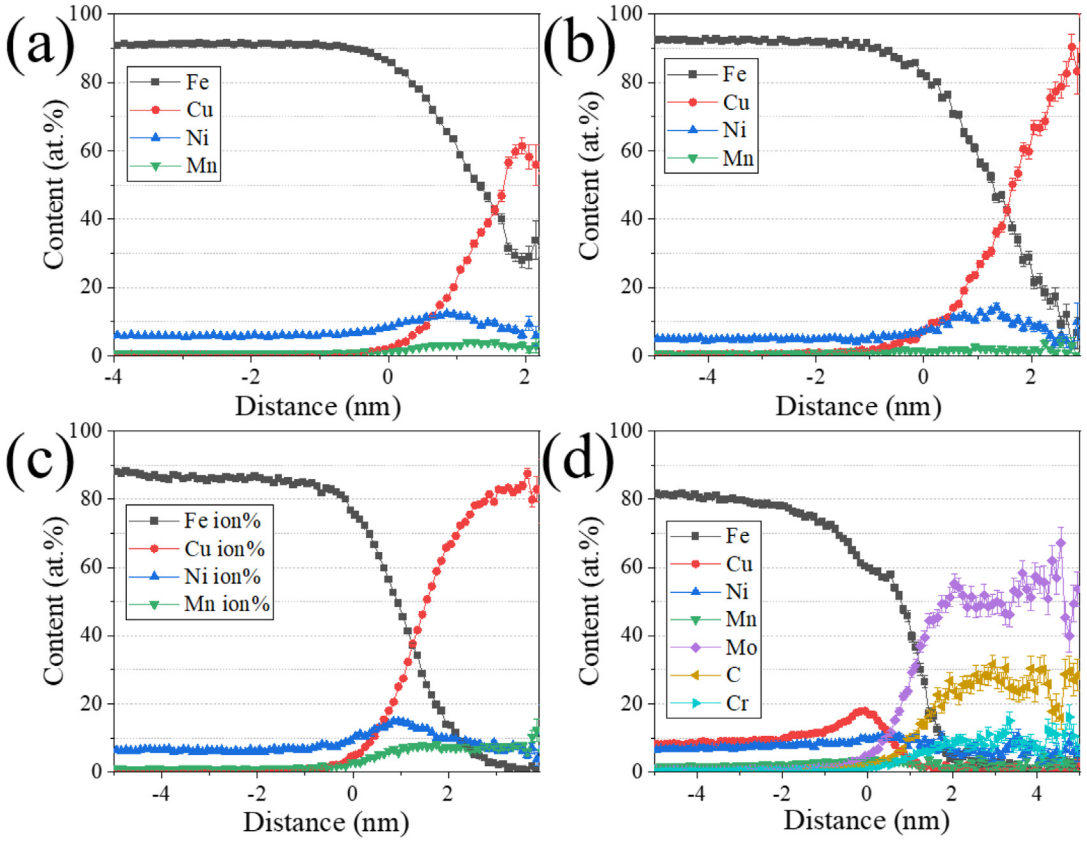

Fig. 13 – Proximity histograms of Cu-precipitates in (a) 500/30 min, (b) 500/100 h, and (c) 550/2 h samples. The proximity histogram of carbides in (d) 500/100 h sample.

4. Discussion

4.1. *Strengthening mechanisms*

The strength origin of the present steel can be approximately rationalized to the strength increments caused by solid-solution strengthening, grain boundary strengthening, dislocation strengthening, and precipitation strengthening. The yield strength of the steel is expressed by Refs. [12,13,25,37,38]:

$$\sigma = \sigma_{GB} + \sigma_{ss} + \sigma_{dislo} + \sigma_{ppt} \quad (2)$$

The equations for the grain boundary strengthening, dislocation strengthening, and solid solution strengthening can be expressed by Refs. [39–41]:

$$\sigma_{GB} = \sigma_0 + k_y d^{-\frac{1}{2}} \quad (3)$$

$$\sigma_{dislo} = M\alpha G b\sqrt{\rho} \quad (4)$$

$$\sigma_{SS} = 4570[C] + 37[Mn] + 83[Si] + 38[Cu] + 11[Mo] - 30[Cr] \quad (5)$$

where σ_0 = 50 MPa is the friction stress [8,38], k_y is the Hall-Petch slope 200 MPa $\mu m^{1/2}$ for martensite packets [37], α equals 0.2 for high dislocation density, M is the Taylor factor 3.0 for BCC metals, G is the shear modulus 80 GPa of the α-Fe matrix, ρ is the GND density, b = 0.25 nm is the Burgers vector, and [Xi] is the content of the element X_i (wt.%) dissolved in the steel. The total strength contribution of grain boundary strengthening, dislocation strengthening and solution strengthening for the 500/30 min, 500/100 h and 550/2 h samples were estimated to be 709, 695, and 732 MPa, respectively.

The strength increment due to the Cu precipitation can be calculated from the particle shear or Orowan dislocation looping. The increase in yield strength by the orowan mechanism is given by Refs. [25,42,43]:

$$\Delta\sigma_{Orowan} = 0.1Gb\frac{f^{1/2}}{R}\ln\frac{R}{b} \quad (6)$$

where R is the average particle radius, f is the volume fraction of the Cu-rich precipitates. The radius and number densities were taken from the APT results. Since the number of Cu precipitates observed in 550/2 h and 500/100 h samples in APT (Fig. 12) is relatively small, the number densities of Cu precipitates in the two states were taken from the TEM results (Fig. 11). The contribution from the Orowan strengthening for the 500/30 min, 500/100 h and 550/2 h samples were estimated to be 276, 175, 238 and MPa, respectively. The M_2C carbides appeared in the 500/100 h sample, which is usually considered to be strengthened by the Orovan mechanism [37,44,45]. The contribution of M_2C carbides is 121 MPa.

Strengthening by particle shearing occurs primarily due to order strengthening, modulus strengthening, and coherency strengthening, which can be estimated as follows [42]:

$$\Delta\sigma_{order} = 0.81M\frac{\gamma_{apb}}{2b}\left[\left(\frac{3\pi f}{8}\right)^{1/2}\right] \quad (7)$$

$$\Delta\sigma_{modulus} = M\frac{Gb}{\lambda}\left[1-\left(\frac{U_P}{U_M}\right)^2\right]^{3/4}\sin^{-1}\left(\frac{U_p}{U_m}\right) \geq 50^\circ \quad (8)$$

$$\Delta\sigma_{coherency} = 4.1MG\varepsilon^{3/2}f^{1/2}\left(\frac{R}{b}\right)^{1/2} \quad (9)$$

where the parameters G, M and b are the same as those in Eq. (9), $\gamma_{apb} = 0.5$ J·m-2 is the average antiphase boundary energy of NiAl [46], $\lambda = 0.866(RN)^{-1/2}$ is the precipitate spacing in the slipe plane, $\varepsilon = 0.35$ J·m^{-2} is the lattice misfit and U_P and U_M are the dislocation line energy in Cu precipitates and α-Fe matrix, respectively. The ratio U_P/U_M depends on the particle radius, R, and is described by Refs. [42,47]:

$$\frac{U_p}{U_m} = \frac{U_p^\infty \log\frac{R}{r_0}}{U_m^\infty \log\frac{r}{r_0}} + \frac{\log\frac{r}{R}}{\log\frac{r}{r_0}} \quad (10)$$

where $r = 2.5$ b and $r_0 = 1000$ r are the inner and outer cut-off radius, respectively, and $U_P/U_M = 0.62$ is the ratio of the energy per unit length of a dislocation in an infinite medium [25]. The contribution from the shearing strengthening for the 500/30 min, 500/100 h and 550/2 h samples were estimated to be 468, 539, and 490 MPa, respectively.

The contributions from each strengthening mechanism, calculated by using the above equations, are summarized in Fig. 14. It can be seen that the shearing mechanism fits well with the tested value for the 500/30 min sample. However, the calculated values of the shearing mechanism are inconsistent with the experimental values of the 550/2 h and 500/100 h samples. This shows that the particle shearing model is only suitable for fine coherent precipitates in the early stage of aging. For the 550/2 h sample, the tested value is between the shearing model and the Orowan model. It is very likely that both mechanisms work in this stage. The calculated value of the Orowan model of the 500/100 h sample is in good agreement with the experimental result, showing that Orowan bypassing mechanism is feasible in this stage.

4.2. *Toughening mechanisms*

The impact toughness of the as-quenched sample is excellent due mainly to the hierarchical structure of lath martensite, which is consistent with the previous research [32,48]. After the aging treatments, the toughness degrades sharply, and the fracture mode changes from ductile fracture to brittle quasi-cleavage fracture (Fig. 3). However, the elongation does not decrease significantly in the low toughness range with no intergranular fracture, indicating that the decrease of toughness is not caused by the segregation of impurity elements at the prior austenite grain boundaries. The size of HAGBs and EGSs and dislocation densities in different aging treatments are almost unchanged, indicating that these are not the main factors leading to the change of toughness. Also, the difference in the composition, such as Mn, Mo and Ni on block and packet boundaries cannot be identified after various aging

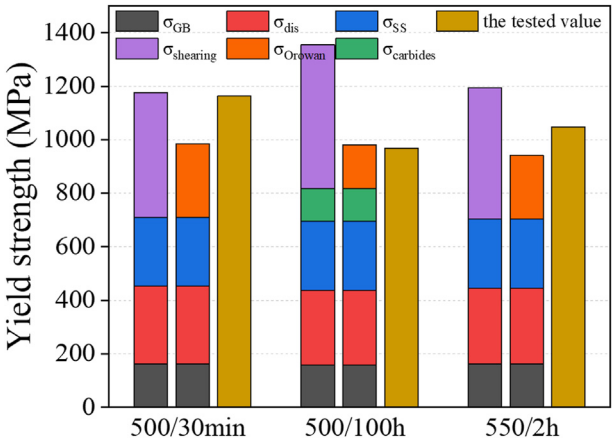

Fig. 14 – Contribution of the various strengthening mechanisms to the total yield strength of the 500/30 min, 500/100 h, and 550/2 h samples.

time. Compared to the 550/2 h and 500/100 h samples, the 550/2 h sample has a higher strength and higher impact energy, indicating that the increase in strength is also not the main reason for the decrease in toughness in this steel.

It can be found in Figs. 6–9 that the contents of solute segregation at the lath boundaries change continuously at the different aging stages. Many studies show that the embrittlement after tempering in steels is related to the impurity segregation at the grain boundaries [49,50]. Mo is considered to be able to effectively enhance the grain-boundary cohesion, preventing a transition from ductile to brittle fracture [30,51]. The segregation of Mn reduces the grain boundary cohesion [49,52–54]. With the decrease of the cohesion at the lath boundary, the crack initiation and propagation become easier, resulting in a low impact energy.

The effect of Mn and Mo segregation at the lath boundary can be measured by the theory proposed by Seah [55]. Assuming that there is no redistribution of solute atoms segregated on the lath boundaries during fracture, the segregation effect on the bonding force at the lath boundary can be evaluated by the pair-bonding between the different atoms. The actual energy required to break the lath boundary bonds can be calculated by calculating the energy per unit area and multiplying them by the total number of lath boundary bonds. For a binary system of solute B in solvent A, the fracture energy of the nearest neighbor bond can be given by:

$$E(0) = -\left(\frac{Z_s}{a_A^2}\right)\varepsilon_{AA} \quad (11)$$

where Z_s is the co-ordination of atoms on one side of the lath boundary with adjacent layers on the other side, a_A^2 is the area of an A atom on the surface, and ε_{AA} is the nearest neighbor bond energies assigned to AA.

The fracture energy of B with a molar fraction X_b at lath boundaries is:

$$E(X_b) = -\frac{Z_s}{a_A^2}\left\{\left(1-\frac{1}{2}X_b\right)^2\varepsilon_{AA} + X_b\left(1-\frac{1}{2}X_b\right)\varepsilon_{AB} + \frac{1}{4}X_b^2\varepsilon_{BB}\right\} \quad (12)$$

Table 3 – The effect of Mn and Mo segregation on fracture energy.

	$X_{Mn}(H_{Fe}^{sub*} - H_{Mn}^{sub*})$ (J/m^2)	$X_{Mo}(H_{Fe}^{sub*} - H_{Mo}^{sub*})$ (J/m^2)	Sum (J/m^2)
500/30 min	10.4	0	10.4
500/100 h	9.9	−4.2	5.7
550/2 h	4.5	−7.1	−2.6

The values of ε_{AA} and ε_{BB} can be determined from the molar sublimation enthalpies:

$$H_A^{sub} = -\frac{1}{2}ZN\varepsilon_{AA}, H_B^{sub} = -\frac{1}{2}ZN\varepsilon_{BB} \quad (13)$$

where N is Avogadro's number and Z is the total co-ordination.

The fracture energy reduction due to segregation can be approximately written as:

$$E(0) - E(X_b) = \frac{Z_s}{Z}X_b\left[H_A^{sub*} - H_B^{sub*}\right] \quad (14)$$

The value of $H^{sub*}\left(=\frac{H^{sub}}{Na^2}\right)$ for Fe, Mn and Mo can be calculated as 13.3, 8.8, and 17.5 J/m^2, respectively. The extra segregation was calculated according to the difference between the peak segregation at the grain boundary and inside the martensite laths of each sample in Fig. 10. The Mn content of the extra segregation at the lath boundary in the 500/30 min, 500/100 h, and 550/2 h samples are 2.3, 2.2, and 1.0 at.%, respectively. The Mo segregation in the 500/30 min, 500/100 h, and 550/2 h samples are 0, 1.0, and 1.7 at.%, respectively. Taking the above values into Eq. (14), the effect of Mn and Mo segregation on the fracture energy can be calculated, as summarized in Table 3.

Since $\frac{Z_s}{Z}$ is a positive number, the larger the total value, the more the decrease in lath boundary cohesion caused by the segregation. The segregation of Mn at the 500/30 min condition significantly deteriorates the lath boundary cohesion, resulting in a low impact toughness. The segregation of Mo at the 550/2 h condition compensates the decrease in the lath boundary cohesion caused by the Mn segregation, which increases the toughness. While due to the decrease of Mo segregation in the 500/100 h condition, Mn again dominates the deterioration of the toughness. Some researchers pointed out that the segregation of Ni at lath boundaries also has a detrimental effect on toughness [56,57], and thus, the high Ni segregation in the 500/100 h samples may have exacerbated its brittle fracture.

5. Conclusions

In this paper, a nano-Cu precipitation-strengthened steel with a combination of high strength, good ductility, and excellent low-temperature toughness were developed by delicately controlling microstructures of the matrix and Cu-precipitates. The evolution of solute segregation at the lath boundaries of martensite and their effects on the low-temperature toughness of a Cu-strengthened steels were thoroughly investigated. The following conclusions can be drawn.

1) The high-strength steel has a combination of ~180 J V-notch impact toughness at −80 °C, ~1050 MPa yield strength, and 19% total elongation.
2) Aging at 500 and 550 °C for different periods of time has little effects on the microstructures of the matrix, including the EGS, dislocation density, martensitic lath size, and the content of high angle grain boundaries.
3) There is no conventional temper embrittlement at 500 and 550 °C for the Cu precipitation-strengthened steel. Mo segregation at the lath boundary can significantly improve the lath boundary cohesion, while Mn segregation can reduce the lath boundary cohesion.
4) The variation of yield strength in the different aging stages is mainly due to the change in precipitation strengthening. The high number density of fine Cu precipitates at the early stage of aging provides a high strength through the shearing mechanism. In the middle stage, due to the growth of Cu precipitates, the strengthening is dominated by the combination of particle shearing and Orowan dislocation looping. In the late stage, coarse Cu precipitates and M_2C contribute to the strength via the Orowan dislocation looping.

Declaration of competing interest

The authors declare that they have no known competing financial interests or personal relationships that could have appeared to influence the work reported in this paper.

Acknowledgments

The present work was supported by the NSFC Funding (U2141207, 52001083, and 52171111), the National Key Research and Development Project (2018YFE0115800, 2020YFE0202600), Youth Talent Project of China National Nuclear Corporation (CNNC2019YTEP-HEU01, CNNC2021YTEP-HEU01), Ansteel Group Corporation project. The atom-probe-tomography research was conducted at the Inter-University three-dimensional (3D) Atom Probe Tomography Unit of City University of Hong Kong supported by the CityU grant 9360161 and CRF grant C1027-14E.

REFERENCES

[1] Wilson A, Hamburg E, Colvin D, Thompson S, Krauss G. Properties and microstructures of copper precipitation aged plate steels. Microalloy HSLA Steels 1988:259–75.
[2] Xu SS, Liu YW, Zhang Y, Luan JH, Li JP, Sun LX, Jiao ZB, Zhang ZW, Liu CT. Precipitation kinetics and mechanical properties of nanostructured steels with Mo additions. Mater Res Lett 2020;8(5):187–94.

[3] Vaynman S, Isheim D, Prakash Kolli R, Bhat SP, Seidman DN, Fine ME. High-strength low-carbon ferritic steel containing Cu-Fe-Ni-Al-Mn precipitates. Metall Mater Trans A 2008;39(2):363–73.
[4] Dhua SK, Ray A, Sarma DS. Effect of tempering temperatures on the mechanical properties and microstructures of HSLA-100 type copper-bearing steels. Mater Sci Eng: A 2001;318(1):197–210.
[5] Czyryca EJ, Link RE, Wong RJ, Aylor DA, Montem TW, Gudas JP. Development and certification of HSLA-100 steel for naval ship construction. Naval Eng J 1990;102(3):63–82.
[6] Graville B. Welding of HSLA (microalloyed) structural steels. ASM 1978;85.
[7] Zhang Z, Liu CT, Miller MK, Wang X-L, Wen Y, Fujita T, Hirata A, Chen M, Chen G, Chin BA. A nanoscale co-precipitation approach for property enhancement of Fe-base alloys. Sci Rep 2013;3(1):1327.
[8] Zhang X, Godfrey A, Huang X, Hansen N, Liu Q. Microstructure and strengthening mechanisms in cold-drawn pearlitic steel wire. Acta Mater 2011;59(9):3422–30.
[9] Jiao ZB, Luan JH, Guo W, Poplawsky JD, Liu CT. Effects of welding and post-weld heat treatments on nanoscale precipitation and mechanical properties of an ultra-high strength steel hardened by NiAl and Cu nanoparticles. Acta Mater 2016;120:216–27.
[10] Jiao ZB, Luan JH, Miller MK, Liu CT. Precipitation mechanism and mechanical properties of an ultra-high strength steel hardened by nanoscale NiAl and Cu particles. Acta Mater 2015;97:58–67.
[11] Jain D, Isheim D, Hunter AH, Seidman DN. Multicomponent high-strength low-alloy steel precipitation-strengthened by sub-nanometric Cu precipitates and M2C carbides. Metall Mater Trans 2016;47(8):3860–72.
[12] Xu S, Zhao Y, Chen D, Sun L, Chen L, Tong X, Liu C, Zhang Z. Nanoscale precipitation and its influence on strengthening mechanisms in an ultra-high strength low-carbon steel. Int J Plast 2019;113:99–110.
[13] Xu SS, Zhao Y, Tong X, Guo H, Chen L, Sun LW, Peng M, Chen MJ, Chen D, Cui Y, Sun GA, Peng SM, Zhang ZW. Independence of work hardening and precipitation strengthening in a nanocluster strengthened steel. J Alloys Compd 2017;712:573–8.
[14] Saha DC, Biro E, Gerlich AP, Zhou Y. Martensite tempering kinetics: effects of dislocation density and heating rates. Mater Char 2020;168:110564.
[15] Kong HJ, Liu CT. A review on nano-scale precipitation in steels. 6(1). 2018. p. 36.
[16] Jiao ZB, Luan JH, Zhang ZW, Miller MK, Ma WB, Liu CT. Synergistic effects of Cu and Ni on nanoscale precipitation and mechanical properties of high-strength steels. Acta Mater 2013;61(16):5996–6005.
[17] Wang LY, Wu YX, Sun WW, Bréchet Y, Brassart L, Arlazarov A, Hutchinson CR. Strain hardening behaviour of as-quenched and tempered martensite. Acta Mater 2020;199:613–32.
[18] Young S-W, Sato M, Yamamitsu K, Shimada Y, Zhang Y, Miyamoto G, Furuhara T. Effect of alloying elements on the high-temperature tempering of Fe-0.3N martensite. Acta Mater 2021;206:116612.
[19] Pietikäinen J. Considerations about tempered martensite embrittlement. Mater Sci Eng: A 1999;273–275:466–70.
[20] Ho P, Mitchell DF, Graham MJ. Surface and grain boundary segregation related to the temper embrittlement of a 214Cr-1Mo steel. Appl Surf Sci 1983;15(1):108–19.
[21] Bulloch JH, Crowe D. Embrittlement observed in Cr–Mo turbine bolts after service. Theor Appl Fract Mech 1998;29(1):59–66.
[22] Materkowski JP, Krauss G. Tempered martensite embrittlement in SAE 4340 steel. Metall Trans A 1979;10(11):1643–51.
[23] Rellick JB, McMahon CJ. Intergranular embrittlement of iron-carbon alloys by impurities. Metall Mater Trans B 1974;5(11):2439–50.
[24] McMahon Jr C, Rellick J, Schulz B. Intergranular embrittlement in ferrous alloys, proceedings of II international conference on fracture. Brighton 1969:23.
[25] Kong HJ, Xu C, Bu CC, Da C, Luan JH, Jiao ZB, Chen G, Liu CT. Hardening mechanisms and impact toughening of a high-strength steel containing low Ni and Cu additions. Acta Mater 2019;172:150–60.
[26] Xie ZJ, Yuan SF, Zhou WH, Yang JR, Guo H, Shang CJ. Stabilization of retained austenite by the two-step intercritical heat treatment and its effect on the toughness of a low alloyed steel. Mater Des 2014;59:193–8.
[27] Kan LY, Ye QB, Wang QH, Tian Y, Wang ZD, Wang YM, Hu J. Refinement of Cu-M2C precipitates and improvement of strength and toughness by Ti microalloying in a Cu-bearing steel. Mater Sci Eng: A 2021;802:140678.
[28] Liu X, Shi Q, Xu M, Kang J, Webb S. Mechanisms of Ti and B on improving weld metal toughness of a Nb-alloyed steel. Mater Sci Eng: A 2020;788:139535.
[29] Li YJ, Ponge D, Choi P, Raabe D. Segregation of boron at prior austenite grain boundaries in a quenched martensitic steel studied by atom probe tomography. Scripta Mater 2015;96:13–6.
[30] Yoo J, Jo MC, Jo MC, Kim S, Kim S-H, Oh J, Sohn SS, Lee S. Effects of solid solution and grain-boundary segregation of Mo on hydrogen embrittlement in 32MnB5 hot-stamping steels. Acta Mater 2021;207:116661.
[31] Ito K, Tanaka Y, Tsutsui K, Omura T. Effect of Mo addition on hydrogen segregation at α-Fe grain boundaries: a first-principles investigation of the mechanism by which Mo addition improves hydrogen embrittlement resistance in high-strength steels,. Comput Mater Sci 2023;218:111951.
[32] Zhao Y, Tong X, Wei XH, Xu SS, Lan S, Wang XL, Zhang ZW. Effects of microstructure on crack resistance and low-temperature toughness of ultra-low carbon high strength steel. Int J Plast 2019;116:203–15.
[33] Chatterjee A, Ghosh A, Moitra A, Bhaduri AK, Mitra R, Chakrabarti D. Role of hierarchical martensitic microstructure on localized deformation and fracture of 9Cr-1Mo steel under impact loading at different temperatures. Int J Plast 2018;104:104–33.
[34] Zhang H, Zhang G, Zhou H, Liu Z, Xu B, Hao L, Sun M, Li D. Influence of cooling rate during cryogenic treatment on the hierarchical microstructure and mechanical properties of M54 secondary hardening steel. Mater Sci Eng: A 2022;851:143659.
[35] Gao H, Huang Y, Nix WD, Hutchinson JW. Mechanism-based strain gradient plasticity—I. Theory. J Mech Phys Solid 1999;47(6):1239–63.
[36] Kubin LP, Mortensen A. Geometrically necessary dislocations and strain-gradient plasticity: a few critical issues. Scripta Mater 2003;48(2):119–25.
[37] Wang JS, Mulholland MD, Olson GB, Seidman DN. Prediction of the yield strength of a secondary-hardening steel. Acta Mater 2013;61(13):4939–52.
[38] Liu T, Cao Z, Wang H, Wu G, Jin J, Cao W. A new 2.4 GPa extra-high strength steel with good ductility and high toughness designed by synergistic strengthening of nano-particles and high-density dislocations,. Scripta Mater 2020;178:285–9.
[39] Zhang X, Hansen N, Gao Y, Huang X. Hall–Petch and dislocation strengthening in graded nanostructured steel. Acta Mater 2012;60(16):5933–43.

[40] Pickering FB. Physical metallurgy and the design of steels. London, U.K.: Applied Science Publishers; 1978. p. 275.
[41] Pan H, Kang R, Li J, Xie H, Zeng Z, Huang Q, Yang C, Ren Y, Qin G. Mechanistic investigation of a low-alloy Mg–Ca-based extrusion alloy with high strength–ductility synergy. Acta Mater 2020;186:278–90.
[42] Russell KC, Brown LM. A dispersion strengthening model based on differing elastic moduli applied to the iron-copper system. Acta Metall 1972;20(7):969–74.
[43] Schnitzer R, Zinner S, Leitner H. Modeling of the yield strength of a stainless maraging steel. Scripta Mater 2010;62(5):286–9.
[44] Wang Y, Sun J, Jiang T, Sun Y, Guo S, Liu Y. A low-alloy high-carbon martensite steel with 2.6 GPa tensile strength and good ductility,. Acta Mater 2018;158:247–56.
[45] Funakawa Y, Shiozaki T, Tomita K, Yamamoto T, Maeda E. Development of high strength hot-rolled sheet steel consisting of ferrite and nanometer-sized carbides. ISIJ Int 2004;44(11):1945–51.
[46] Povoden-Karadeniz E, Kozeschnik E. Simulation of precipitation kinetics and precipitation strengthening of B2-precipitates in martensitic PH 13–8 Mo steel. ISIJ Int 2012;52(4):610–5.
[47] Lloyd DJ. Precipitation hardening. In: McQueen HJ, Bailon JP, Dickson JI, Jonas JJ, Akben MG, editors. Strength of metals and alloys (ICSMA 7). Pergamon; 1986. p. 1745–78.
[48] Wei X, Cao X, Luan JH, Jiao ZB, Liu CT, Zhang ZW. Synergy of strengthening and toughening of a Cu-rich precipitate-strengthened steel. Mater Sci Eng: A 2022;832:142487.
[49] Kuzmina M, Ponge D, Raabe D. Grain boundary segregation engineering and austenite reversion turn embrittlement into toughness: example of a 9 wt.% medium Mn steel. Acta Mater 2015;86:182–92.
[50] Kawakubo T, Ushioda K, Fujii H. Grain boundary segregation and toughness of friction-stir-welded high-phosphorus weathering steel. Mater Sci Eng: A 2022;832:142350.
[51] Jo MC, Yoo J, Kim S, Kim S, Oh J, Bian J, Sohn SS, Lee S. Effects of Nb and Mo alloying on resistance to hydrogen embrittlement in 1.9 GPa-grade hot-stamping steels. Mater Sci Eng: A 2020;789:139656.
[52] Inoue T, Yamamoto K, Sekiguchi S. Grain boundary segregations of phosphorus and manganese in low carbon manganese steels. Trans Iron Steel Inst Jpn 1974;14(5):372–4.
[53] Zhong L, Wu R, Freeman AJ, Olson GB. Effects of Mn additions on the P embrittlement of the Fe grain boundary. Phys Rev B 1997;55(17):11133–7.
[54] Yang R, Zhao DL, Wang YM, Wang SQ, Ye HQ, Wang CY. Effects of Cr, Mn on the cohesion of the γ-iron grain boundary. Acta Mater 2001;49(6):1079–85.
[55] Seah MP. Adsorption-induced interface decohesion. Acta Metall 1980;28(7):955–62.
[56] Hu Y-J, Wang Y, Wang WY, Darling KA, Kecskes LJ, Liu Z-K. Solute effects on the Σ3 111[11-0] tilt grain boundary in BCC Fe: grain boundary segregation, stability, and embrittlement. Comput Mater Sci 2020;171:109271.
[57] Mai HL, Cui X-Y, Scheiber D, Romaner L, Ringer SP. The segregation of transition metals to iron grain boundaries and their effects on cohesion,. Acta Mater 2022;231:117902.